Applied Catalysis B: Environmental 340 (2024) 123167

Contents lists available at ScienceDirect

Applied Catalysis B: Environmental

journal homepage: www.elsevier.com/locate/apcatb

Photoelectrochemical water oxidation using hematite modified with metal-incorporated graphitic carbon nitride film as a surface passivation and hole transfer overlayer

Tae Hwa Jeon [a], Cheolwoo Park [b], Unseock Kang [c], Gun-hee Moon [d], Wooyul Kim [b], Hyunwoong Park [c,*], Wonyong Choi [b,*]

[a] SK Innovation Co., 325 Exporo, Yuseong-gu, Daejeon 34125, Republic of Korea
[b] KENTECH Institute for Environmental and Climate Technology, Korea Institute of Energy Technology (KENTECH), Naju 58330, Republic of Korea
[c] School of Energy Engineering, Kyungpook National University, Daegu 41566, Republic of Korea
[d] Extreme Materials Research Center, Korea Institute of Science and Technology, Seoul 02792, Republic of Korea

ARTICLE INFO

Keywords:
Carbon nitride
Metal incorporation
Photoelectrochemical water splitting
Junction structure
Hole-mediating interlayer

ABSTRACT

Hematite (α-Fe_2O_3) is renowned as a promising photoanode for water oxidation, even though it displays poor photoconversion efficiency. In this study, ~5 nm-thick graphitic carbon nitride (g-C_3N_4; CN) and metal-incorporated CN (M-CN; M = Ag, Fe, Co) films are uniformly deposited on hematite via a facile one-step evaporation method. Herein, the Co-CN layer leads to the highest photoelectrochemical activity with hematite-based photoanode. The subsequent loading of Co-CN layer with oxygen evolution catalysts (FeNiOOH and CoOOH) further enhances photocurrent density to ~3.5 mA cm^{-2} and oxygen evolution at > 95 % of Faradaic efficiency over 24 h at E = 1.23 V. Detailed analysis based on spectroscopic and electrochemical measurements demonstrate that the primary role of CN layer is improving the charge separation efficiency by passivating the hematite surface. Then the incorporated metals contribute to reducing charge transfer resistance and thereby mediating hole transfer to interfacial water.

1. Introduction

Photoelectrochemical (PEC) water splitting is a promising approach to convert sunlight into storable chemical fuels (e.g., H_2) [1–4]. The overall efficiency of the PEC system primarily depends on a photoanodic reaction (i.e., water oxidation reaction) that is associated with generating the proton and electron pairs. Unfortunately, the water oxidation reaction is kinetically sluggish and requires a large overpotential. This eventually reduces the hydrogen production, and thereby leading to limit the overall photoconversion efficiency. Addressing this issue, a great deal of effort has been expended in recent times to develop the cost-effective, ultra-efficient oxide photoanodes with suitable energy levels and enhanced durability (e.g., WO_3 [5–8], $BiVO_4$ [9–11], and α-Fe_2O_3) [12–15].

Among them, α-Fe_2O_3 (hematite) is considered the most ideal photoanode material because of absorption of broadband sunlight (λ ~600 nm; E_g ~2.1 eV) and theoretically high solar-to-hydrogen efficiency (~15 %) [13,16–18]. However, its intrinsically low electrical conductivity and short diffusion length of the minority carriers (2–4 nm) causes inefficient charge separation and injection processes [2,9–12], leading to the actual efficiency of < 7 % [13,19–23]. To address the challenge, the physicochemical property of hematite itself (e.g., morphology [13,24,25] and doping [13,25–30]) was altered and the hematite surface was modified with passivation layer [31–34]. Particularly, the surface passivation with ultra-thin amorphous oxide layers (e.g., Al_2O_3 and TiO_2) effectively minimizes the exposure of the surface trap sites working as charge recombination centers and facilitates the interfacial charge transfers [13,35,36]. For uniform passivation, the dry deposition (e.g., atomic layer deposition and electron beam evaporation) has been considered. However, choosing suitable oxide materials is not easy because of the limited precursors available in the processes. Solution-processed adsorption and impregnation of precursors was also employed. Unfortunately, the uniform, pinhole-free deposition remains challenges and the following annealing step is usually required to transform the adsorbed precursors into oxides.

Alternative to the oxides, graphitic carbon nitride (g-C_3N_4 or CN)

* Corresponding authors.
E-mail addresses: hwp@knu.ac.kr (H. Park), wchoi@kentech.ac.kr (W. Choi).

https://doi.org/10.1016/j.apcatb.2023.123167
Received 19 June 2023; Received in revised form 8 August 2023; Accepted 10 August 2023
Available online 12 August 2023
0926-3373/© 2023 Elsevier B.V. All rights reserved.

was considered as a non-oxide passivation material. Although bulky g-C_3N_4 has some photocatalytic and photoelectrochemical activity [37–40], an ultra-thin, transparent g-C_3N_4 film minimizes contribution to the photocurrent generation, decoupling the passivation effect from mixed PEC activity [41–43]. It is further noted that CN can serve as a platform for immobilizing functional metals. Some metal ions were incorporated into the CN networks to mediate the valence band holes and facilitate interfacial charge transfers [38,39,44–46]. This suggests that the metal-incorporated CN (M-CN) layer has a dual function of surface passivation and hole transfer mediation (Scheme 1). With this in mind, we synthesized hematite electrodes modified with CN and M-CN as hole-mediating layers via a one-step evaporation method [18,47]. In the preliminary study, four CN precursors (cyanamide, dicyandiamide, melamine, and urea) and ten metal precursors (Ru, Zn, Sn, Mn, Ce, Ni, Cu, Ag, Fe, and Co) were tested for the PEC water oxidation using hematite film electrodes. Among the combinations, the cyanamide-oriented CN with Ag(I), Fe(III), and Co(II) ions were found to significantly enhance the O_2 evolution rate and faradaic efficiency. Mn, Ce, Ni, and Cu were also relatively effective, whereas Ru, Zn, and Sn were inactive. These different effects were attributed to one-electron oxidation potentials with respect to the hematite valence band. Various physicochemical and photoelectrochemical analyses were performed and the PEC activity was maximized with assistance of oxygen evolving catalysts.

2. Experimental

2.1. Synthesis of bare and modified hematite electrodes

All reagents and chemicals of analytical grade were purchased from Sigma-Aldrich and used without further purification unless otherwise specified. Thin-film hematite (α-Fe_2O_3; F) electrodes were synthesized using a spin-coating method. Typically, 0.1 M $FeCl_3 \cdot 6\,H_2O$ (97 %) was dissolved in ethanol (J.T. Baker, 99.9 %) containing concentrated HCl to prevent the precipitation of Fe(III) ions. 0.01 M $Ti(OBu)_4$ (97%) was additionally dissolved in the solution at 10 at% with respect to Fe to improve electrical conductivity of hematite. The precursor solution was dropped to fluorine-doped tin oxide (F-SnO_2: FTO, 10 mm × 30 mm, Pilkington Co., Ltd.) substrates at 35 μL cm^{-2} and spread at 3000 rpm for 30 s, followed by annealing at 350 °C for 10 min. This coating-annealing cycle was repeated up to 10 times, and then the samples were annealed at 550 °C for 1 h.

Graphitic carbon nitride (g-C_3N_4; CN) was deposited onto bare FTO substrates and hematite electrodes via an evaporation method [48].

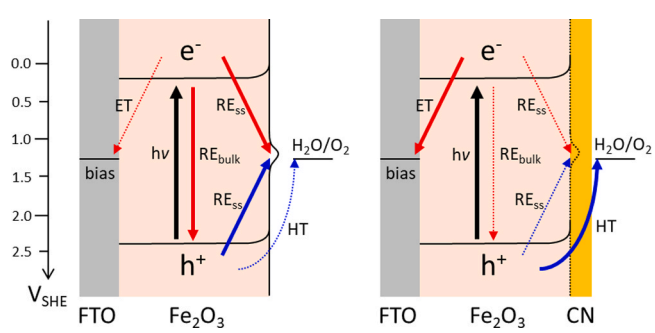

Scheme 1. Photo-induced charge transfer mechanisms with (a) bare and (b) modified hematite films. For bare hematite, most of the photogenerated charge carriers recombine in the bulk and at the surface trap sites. Even under potential bias, a significant fraction of holes is trapped, thus reduces the hole-mediated water oxidation reaction. In the presence of CN layer, the surface trap sites are effectively passivated. When metal ions are incorporated into the CN network, the transferred holes oxidize the metal ions into high-valent states, responsible for water oxidation reaction. ET, HT, RE, and SS refer to electron transfer, hole transfer, recombination, and surface trap sites, respectively.

Typically, cyanamide (Alfa Aesar, >98%) of 20–200 mg was dissolved in an alumina crucible cover (diameter: 55 mm) containing deionized water (18 MΩ cm) and dried at 80 °C for 1 h. Then, the hematite samples were placed in the alumina crucible and covered by the as-prepared crucible cover. The crucible was annealed at 550 °C for 20 min at a ramping rate of 10 °C min^{-1}. Instead of cyanamide, other CN precursors (dicyanamide, melamine, and urea) were also tested. For M-CN layer, $RuCl_3 \cdot xH_2O$ (99.98 %), $Zn(NO_3)_2 \cdot 6\,H_2O$ (98 %), $SnCl_4$ (98 %), $MnCl_2 \cdot 4\,H_2O$ (98 %), $Ce(NO_3)_3 \cdot 6\,H_2O$ (99 %), $NiCl_2$ (98 %), $CuCl_2 \cdot 2\,H_2O$ (99 %), $AgNO_3$ (99.0 %), $Fe(NO_3)_3 \cdot 9\,H_2O$ (99.0 %), and $Co(NO_3)_2 \cdot 6\,H_2O$ (98 %) were added to cyanamide solutions at 0.1–5 wt% (normally 1 wt%, unless otherwise specified). For comparison, bare CN powders were obtained via annealing cyanamide powder in the crucible cover at 550 °C for 20 min at a ramping rate of 10 °C min^{-1}. For the synthesis of metal-doped CN powders, appropriate amounts of metal precursor powder (1 wt%) and cyanamide power were ground together and annealed under the same conditions as those for the CN powder.

Cobalt oxyhydroxide (CoOOH) and iron-nickel oxyhydroxide (FeNiOOH) cocatalysts were further loaded on the as-synthesized hematite electrodes with cobalt-incorporated g-C_3N_4 (Co-CN) overlayer via photodeposition and drop-casting method, respectively. In the former, the sample electrodes were immersed in aqueous solutions of 0.1 M potassium phosphate buffer (pH 7) containing 0.5 mM $CoCl_2 \cdot 6\,H_2O$ (98%) and irradiated under AM 1.5 G (1 sun) for 30 min [13]. The as-obtained cobalt phosphate complexes were changed to CoOOH during photoelectrochemical anodic reactions in alkaline solutions. To deposit FeNiOOH, a precursor solution containing 4 mM $FeCl_3 \cdot 6\,H_2O$ (97 %) and 6 mM $NiCl_2 \cdot 4\,H_2O$ (98%) in ethanol (J. T. Baker, 99.9 %) was prepared. The precursor solution was dropped on electrodes at 10 μL cm^{-2}. After drying in air, the electrodes were immersed in 0.1 M KOH for 10 s [26,49].

2.2. Photoelectrochemical activity measurements

The PEC behavior of the as-synthesized samples (working electrode, geometric area of 0.5 cm^2) were examined with Ag/AgCl electrode (reference electrode) and Pt wire (counter electrode) in a single-compartment cell containing 1 M KOH solution pre-purged with Ar (99.9 %) for 30 min. Linear sweep voltammograms (LSVs) were obtained by sweeping potential from − 0.2–0.6 V vs. Ag/AgCl at a scan rate of 10 mV s^{-1} using an electrochemical workstation (VersaSTAT 3–400, Princeton Applied Research) in the dark or under AM 1.5 G light (100 mW cm^{-2}; Oriel). For chronoamperometry, a constant potential of 0.23 V vs. Ag/AgCl (equivalent to 1.23 V vs. reversible hydrogen electrode) was applied to the working electrode. Electrochemical impedance spectroscopy (EIS) for sample electrodes was conducted at 0.23 V vs. Ag/AgCl with an AC voltage of 10 mV and a frequency range of 0.1 kHz and 0.01 Hz. The charge injection and separation efficiencies for sample electrodes were estimated using LSVs recorded in 1 M KOH solution containing 0.1 M H_2O_2 (Junsei, 35 %), as described in detail elsewhere [9]. Applied or measured potential values with respect to Ag/AgCl were converted to potential values versus reversible hydrogen electrode (RHE) by the following: V vs. RHE = V vs. Ag/AgCl + 0.0591 × pH + 0.197. Incident photon-to-current efficiency (IPCE) was estimated at a constant potential of 0.23 V vs. Ag/AgCl using a CS 130 monochromator (Newport) with a 10-nm bandpass under irradiation by a 300 W Xe arc lamp (Newport Oriel). The IPCE values were calculated using the following: IPCE (%) = $(1240 \times J_{ph}) \times 100 / (P \times \lambda)$, where J_{ph}, P, and λ refer to the photocurrent density, photon flux, and wavelength, respectively. The headspace gaseous products (O_2 and H_2) in the cell were quantified using a gas chromatography (GC, HP6890A) equipped with a thermal conductivity detector and a 5 Å molecular sieve column. Prior to irradiation, the solutions were purged with Ar gas in the reactor for 30 min to remove dissolved oxygen. Hereafter, "vs. RHE" is omitted for simplicity in describing potential values, unless otherwise mentioned.

2.3. Surface characterization

The morphology of samples was analyzed by high-resolution scanning electron microscopy (HR-SEM; JEOL JSM-7401 F), high-resolution transmission electron microscopy (HR-TEM; JEM-2200F), and electron energy loss spectroscopy (EELS) using a Cs-corrected line at the National Institute for Nanomaterials Technology (Pohang, Korea). The surface elemental composition and chemical analysis were conducted by X-ray photoelectron spectroscopy (XPS; Theta Probe AR-XPS System) using monochromated Al Kα radiation as an X-ray source (1486.6 eV) at the Korea Basic Science Institute (Pusan center, South Korea). Grazing incident X-ray diffraction (XRD) patterns were obtained using Cu Kα radiation (RIGAKU D MAX 2500). The UV–visible absorption spectra of samples were obtained using a spectrophotometer (Shimadzu UV-2401PC). The surface functional groups of samples were analyzed by Attenuated Total Reflectance Fourier Transform Infrared Spectroscopy (ATR-FTIR; Thermo Scientific iS50) using ZeSe crystal with a scan number of 100. Photoluminescence (PL) emission spectra were obtained using a fluorescence spectrophotometer (Shimadzu RF-5301). Fluorescence lifetime decays were measured by an inverted-type scanning confocal microscope (MicroTime-200, Picoquant, Germany) with a 20 × objective. The measurements were performed at the KBSI (Daegu center, South Korea). A single-mode pulsed diode laser (375 nm) was used as an excitation source and fluorescence decay curves were obtained at 405 nm to collect emissions from the samples. Exponential fittings for the obtained fluorescence decays were performed using the Symphotime software (version 5.3). Transient absorption measurements were conducted to investigate charge carrier dynamics using the third harmonic of the Nd:YAG laser (10 Hz, NT342A, EKSPLA, λ = 355 nm, 1.5 mJ/pulse) as the pump source and a continuous Xenon (Xe) lamp (300 W, Newport) as the probe source. The probe beam was directed through a monochromator (SP-2300, Acton) and detected using a photomultiplier tube (PDS-1, Dongwoo Optron), which was electrically connected to a preamplifier (SR445A, Stanford Research Systems, Inc.) and a digital oscilloscope (MDO4034C, Tektronix, 350 MHz). All measurements were performed at room temperature with the pump-probe beams overlapping with the Ti-doped hematite films on FTO glasses.

3. Results and discussion

3.1. Surface characterizations of hematite and g-C_3N_4

The XRD pattern with a hematite film deposited with g-C_3N_4 (F/CN) was examined (Fig. 1a). All the marked XRD peaks at 2θ = 24.1° (012), 33.4° (104), 35.7° (110), 49.5° (024), 57.8° (018), and 62.6° (214) were assigned to a typical α-Fe_2O_3 (JCPDS No. 33–0664). The unmarked peaks resulted from SnO_2 (JCPDS No. 77–0452) of the substrate [13,50]. The crystalline structure of CN deposited on the hematite was not observed. In contrast, the as-synthesized CN and Co-incorporated CN (Co-CN) powders exhibited the typical g-C_3N_4 peaks at 2θ = 13.3° (100) and 27.3° (002) (JCPDS Ref. No. 87–1526). Hence, the absence of CN in the F/CN should be attributed to insufficient amount (i.e., thinness) of CN for XRD analysis.

The formation of CN on hematite was further examined by FTIR and XPS. The FTIR spectrum of the CN powder showed the typical characteristic absorption bands for bending vibration mode of triazine units (ν = 800 cm^{-1}), stretching vibration modes of C−N heterocycle (ν = 1200–1700 cm^{-1}), and stretching vibrations of C−N − H (amino component originated from the terminal amino groups, ν = 2800–3500 cm^{-1}) (Fig. 1b). The residual amino component in the CN powder was typically attributed to the incomplete condensation of precursor during the thermal pyrolytic process. Among the absorption bands, the stretching vibration modes of the C−N heterocycle were observed in F/CN and F/Co-CN samples, indicating presence of CN on hematite surface (Fig. S1 for other F/M-CN samples). The XPS spectra with F/CN and F/Co-CN samples also showed the characteristic carbon bands at binding energy of ~288 eV, which was attributed to *sp2* carbon in tris-s-triazine rings (N = C−N) (Fig. 1c). This *sp2* carbon band slightly shifted to low binding energy by 0.1 eV upon Co loading, indicating that Co was incorporated into the CN framework. The same behavior by Co loading was observed for CN powder (Fig. 1d). The bands at ~284.5 eV in the C1s XPS spectra belonged to adventitious carbon contaminants (Fig. S2). The N 1 s XPS spectra with CN and Co-CN powders also showed N 1 s bands at ~398 eV, which were deconvoluted into C−N = N band (398.2 eV), N − $(C)_3$ band (~400 eV), C−N − H band (400.8 eV), and π-excitation (~404 eV) (Fig. 1e). Co-CN powder exhibited Co 2p bands at ~796 eV (Co 2p1/2) and ~780 eV (Co 2p3/2) (Fig. 1f). Their intensities were not high enough due to a low fraction (1%) of Co with respect to CN. Nevertheless, the observed bands could

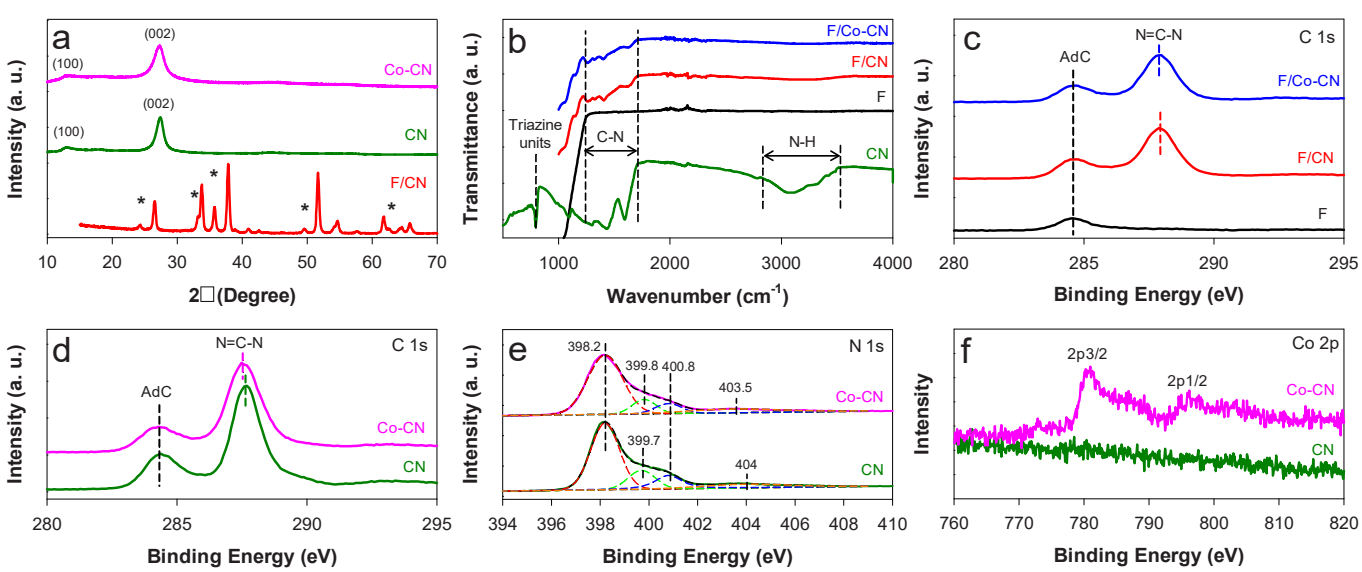

Fig. 1. Surface characterizations of bare and modified samples (film and powder types). (a) XRD patterns. * represents crystalline phases of hematite. (b) FTIR spectra. (c and d) C1s XPS spectra with films and powders, respectively. AdC refers to adventitious carbon. (e) N1s XPS spectra. (f) Co 2p XPS spectra. CN and Co-CN represent powders. F/CN and F/Co-CN refer to hematite (F) deposited with CN and Co-CN, respectively.

be assigned as Co(II) state, indicating that the oxidation state of Co precursor was maintained. Other metals (Fe and Ag) also maintained their original oxidation states (Fig. S3).

The bare hematite showed porous structures composed of nanoparticle aggregates (Fig. 2a). In contrast, the CN-deposited hematite displayed compact and less porous surface (Fig. 2b). Hematite samples with M-CN (e.g., Co-CN, Fe-CN, and Ag-CN) also showed the similar surface morphologies with those with CN (Fig. 2c and S4). A cross-sectional SEM image with F/CN displayed clear formation of 150–200 nm-thick hematite film, whereas CN adlayer was not visible in the image (Fig. 2d). A Co-CN adlayer was also not observed for F/Co-CN sample (Fig. S5). To estimate the CN layer thickness, cross-sectional elemental mappings with bare and CN-modified hematite films were compared (Fig. 2e). For the bare hematite, Fe and O atoms were found from the topmost surface and the Sn atoms resulting from the FTO substrate gradually appeared from a depth of ~50 nm. The doped Ti atoms were also found concurrently with the Fe atoms, confirming uniform intercalation into the hematite lattice. For the F/CN sample, both C and N atoms were found only within ~10 nm-depth, where the fractions of Fe, O, and Ti atoms were relatively low because of the C and N atoms. This elemental distribution configuration demonstrates that ultrathin CN layer (<10 nm) was deposited well onto hematite surface. The heterojunction structure of hematite and Co-CN was further examined using cross-sectional HR-TEM analysis (Fig. 3a). The HR-TEM analysis obviously displayed the uniform ~5 nm-thick Co-CN layer on the hematite surface. All composition elements (Fe, O, Ti, C, N, and Co) were also found, confirming the Co-CN layer on the hematite. For further analysis of the heterojunction structure, F/Co-CN particles were collected from FTO substrate. All composition elements of the F/Co-CN films (Fe, O, Ti, C, and Co) were also found in the F/Co-CN particles (Fig. 3b), with lattice fringes of 0.277 and 0.340 nm matching α-Fe_2O_3 (104 plane) and g-C_3N_4 (002 plane), respectively (Fig. 3c).

3.2. Photoelectrochemical activities of bare and modified hematite electrodes

LSVs with the as-synthesized bare and modified hematite electrodes were obtained 1 M KOH under irradiation (Fig. 4a). The bare hematite electrode exhibited a relatively low photocurrent density (J_{ph}) of ~0.5 mA cm^{-2} at 1.23 V, with an onset potential (E_{on}) of 0.95 V. This J_{ph} value was lower than that with nanorod-structured hematite electrodes [13]. Typically, the nanorod structures lead to relatively high J_{ph} due to radial-directional charge transfer. However, such 2-dimensional structures are intrinsically difficult for complete passivation. Deposition of CN to the as-synthesized hematite film enhanced J_{ph} by two times (~1 mA cm^{-2}) at 1.23 V. Excess amounts of CN reduced the PEC activity of hematite (Fig. S6) because of inhibited hole transfer to water through the thick CN layer. Other CN films oriented from different precursors (melamine, dicyandiamide, and urea) generated similar and yet less pronounced effects (Fig. S7), presumably due to relatively unfavorable structures for metal incorporation and charge transfers. Incorporation of metal into CN further increased J_{ph} in the following order: Co (2.5 mA cm^{-2}) > Fe (2.4 mA cm^{-2}) > Ag (1.8 mA cm^{-2}). However, E_{on} was not significantly altered by the CN deposition and metal incorporation, indicating that the primary role of the CN and M-CN was to facilitate the charge transfer kinetics with hematite [2,9,10,13,51–53]. IPCE profiles were also obtained at 1.23 V (Fig. 4b). For all samples, IPCE onset was ~600 nm due to E_g of hematite (~ 2.1 eV) [13,24]. The bare hematite showed poor IPCE values (e.g., ~1.7 % at λ = 420 nm). Fe-CN and Co-CN significantly improved IPCE values up to ~9 % at λ = 420 nm. Ag-CN generated a similar yet less pronounced effect.

The roles of CN and M-CNs were speculated to enhance light

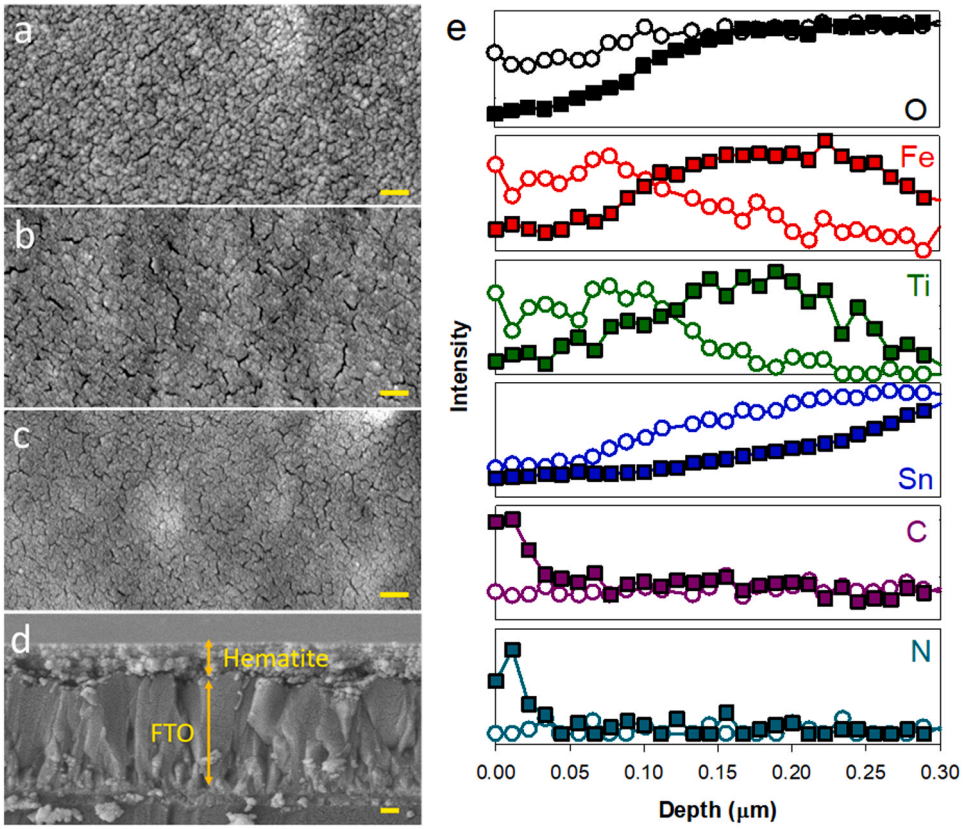

Fig. 2. (a-c) SEM images (top views) of bare, CN-deposited, and Co-CN-deposited hematite surfaces, respectively. (d) A cross-sectional SEM image of CN-deposited hematite. Each bars in a-d represent length of 100 nm. (e) Cross-sectional elemental mappings with bare hematite (F, open symbols) and CN-deposited hematite (F/CN, closed symbols) for O, Fe, Ti, Sn, C, and N. For both samples, Ti(IV) was doped into hematite to improve the electrical conductivity.

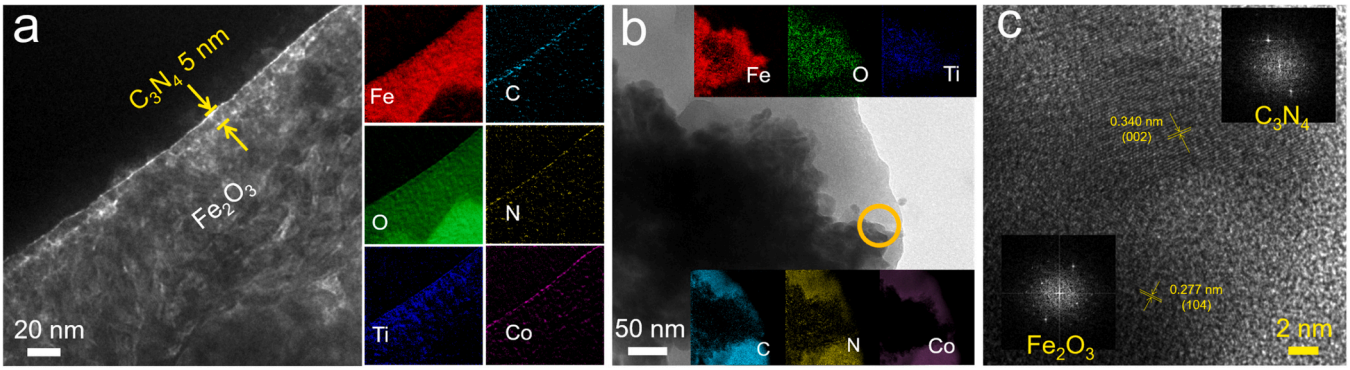

Fig. 3. (a) Cross-sectional HR-SEM image and EELS elemental mappings for an F/Co-CN film sample. For all hematite samples, Ti(IV) was doped to improve the electrical conductivity. (b and c) TEM and HR-TEM images for F/Co-CN particles. Fig. 3b inset shows EELS mapping of Fe, O, Ti, C, N, and Co. Fig. 3c inset shows the electron diffraction patterns of F and CN.

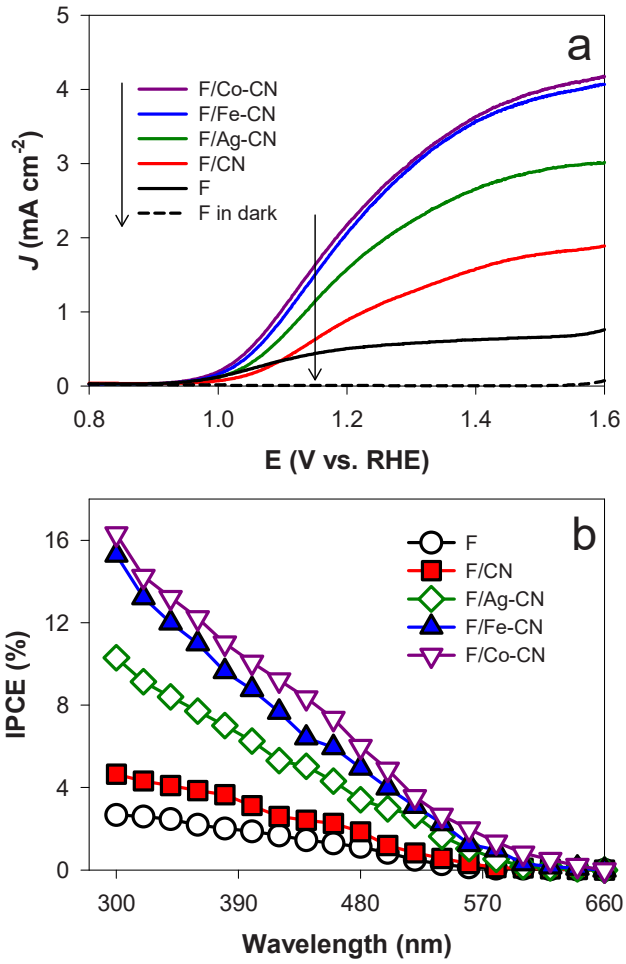

Fig. 4. Photoelectrochemical behavior of bare and modified hematite electrodes in 1 M KOH solutions at pH ~13.6. (a) Linear sweep voltammograms. (b) IPCE profiles at E = 1.23 V.

absorption, charge separation, and charge injection. To examine the first possibility, the absorbance spectra of bare and modified hematite films were compared (Fig. 5a). All the hematite films displayed broad absorption bands in the wavelength range of 300–600 nm. The same absorption onsets (λ_{on} ~600 nm) among the samples indicates the same E_g values of ~2.1 eV. The λ_{on} values were similar to those of IPCE onset, confirming that the J_{ph} generation resulted solely from photon absorption. Slightly different absorption intensities were attributed to the physical states of each film (e.g., thickness and topography). Meanwhile, a CN film itself (i.e., without hematite) did not generate J_{ph} at $E < 1.5$ V; however, large dark currents flowed from $E > 1.5$ V (Fig. 5a inset). A Co-CN film exhibited the same behavior. These results indicate the insignificant effects of CN and M-CN on the photo-induced charge generation phenomenon with hematite electrodes.

In contrast, CNs were found to significantly influence charge separation and injection efficiencies (η_{sep} and η_{inj}, respectively) with hematite [9,13,24]. These efficiencies were estimated using H_2O_2 as a hole scavenger (Fig. S8). For all electrodes, η_{sep} increased rather linearly with increasing E to ~1.3 V (Fig. 5b). It appeared that the band-bending was not still enough even at $E = 1.3$ V to fully suppress charge recombination. Notably, a bare hematite had η_{sep} of ~17% at 1.23 V, which increased to ~26% and 32% upon CN and M-CN deposition, respectively. These η_{sep} values were higher than those with hematite films directly modified with metal catalysts [24,54]. It appears that the incorporated metal was less influential than CN itself in enhancing η_{sep}. One of the most effective ways to improve η_{sep} is to shorten the charge transfer path under a given absorption and charge generation efficiencies. Two-dimensional structures (e.g., wires [51–53], rods [5,13, 55,56], and tubes [12,57–59]) have been proved for high η_{sep}. For example, a modified hematite nanorod electrode exhibited η_{sep} of ~55 % at 1.23 V [13]. M-CNs also enhanced η_{inj}, such to ~66 % at 1.23 V with F/Co-CN and F/Fe-CN (Fig. 5c). In contrast, η_{inj} values with F/CN were quite similar to those with F. Hence, the primary role of CN should improve η_{sep} by passivating hematite surface and effectively blocking surface trap sites working as recombination centers. Meanwhile, metal ions incorporated into CN worked as (immobilized) catalysts for interfacial hole transfer.

The CN and M-CNs were also found to significantly improve electrical conductivity of hematite electrodes (Fig. 5d). The Nyquist plot with bare hematite showed a large semicircle, which gradually decreased in diameter with deposition of CN and M-CNs. Fitting the semicircles into the Randle circuit produced the interfacial charge transfer resistance (R_{ct}) values of ~6, 1.3, and 0.55 kΩ for F, F/CN, and F/Co-CN, respectively (Fig. S9). The different R_{ct} values should primarily result from CN and M-CN overlayers because of the same hematite. The charge transfer dynamics with CN and M-CNs were further examined using PL and TRPL analysis (Fig. S10 and Fig. 5d inset). Upon excitation at $\lambda = 375$ nm, a broad emission band at λ ~400 nm was observed with CN. This band was attributed to the HOMO-LUMO (or bandgap) recombination of charge carriers. M-CNs also showed similar emission bands, yet with reduced intensities (CN > Ag-CN > Fe-CN > Co-CN). This indicates that the incorporated metals could intrinsically inhibit charge recombination and cobalt exerted the greatest effect. TRPL analysis further revealed that the average decay lifetime of charge carriers was 3.09 ns for CN, which decreased to 3.07 ns, 2.48 ns, and 2.26 ns with Ag-CN, Fe-CN, and Co-CN, respectively.

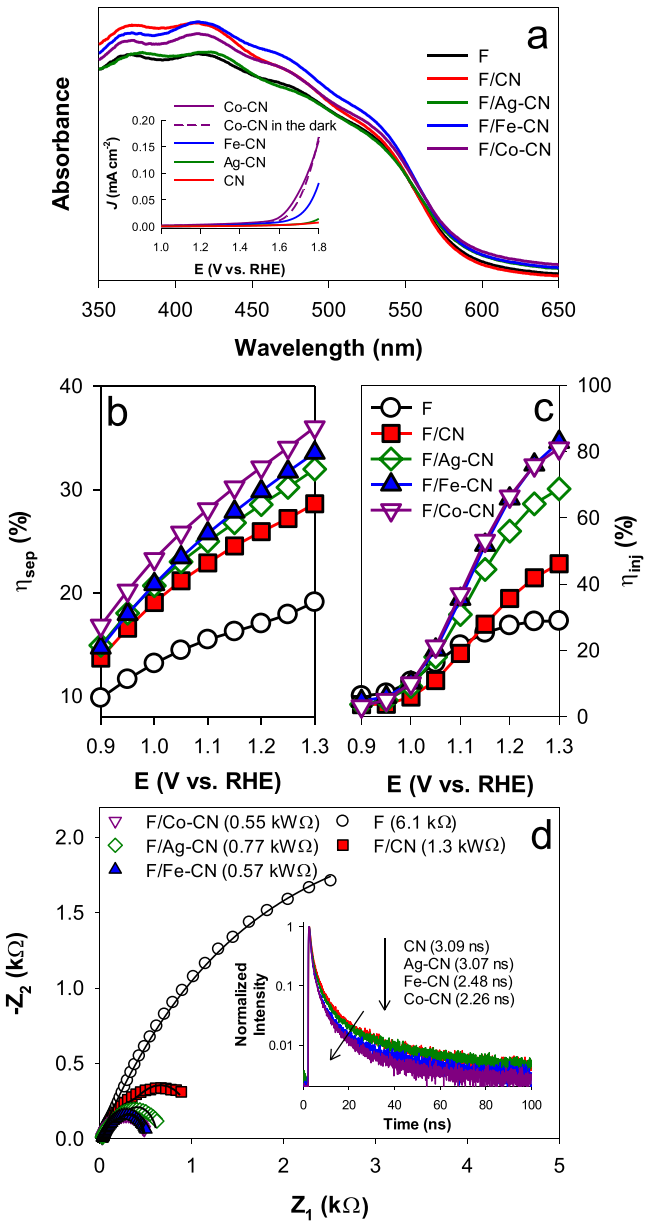

Fig. 5. (a) UV–vis absorption reflectance spectra of bare and modified hematite films. Inset shows linear sweep voltammograms with CN and M-CN films (without hematite) at E = 1.23 V under irradiation or in the dark. (b and c) Charge separation and injection efficiencies (η_{sep} and η_{inj}, respectively) with bare and modified hematite electrodes. (d) Nyquist plots with bare and modified hematite electrodes at E = 1.23 V. Inset shows TRPL decay spectra with CN and M-CN powders. Numbers in parentheses indicate the charge transfer resistance and average decay lifetimes of charge carriers.

Both Nyquist and TRPL analyses reveal the intrinsic role of CN in passivating the defect surface of hematite. The incorporated metals further contributed to reducing R_{ct}, thereby enhancing hole transfer to interfacial water. To further examine the role of the incorporated metals on the photogenerated charge carrier kinetics, TAS analysis was conducted for bare and Co-CN-modified hematite films excited by $\lambda = 355$ nm in the nanosecond to microsecond-time scales. The nanosecond TAS provides information on the excited state dynamics of hematite films treated with different surface modifications [60–62]. The bare hematite exhibited trapped holes at $\lambda = 500$–650 nm, which is consistent with previous reports (Fig. S11). To eliminate the effect of photoluminescence, the normalized lifetime of trapped holes was analyzed for hematite at $\lambda = 600$ nm (Fig. 6). Compared to the bare

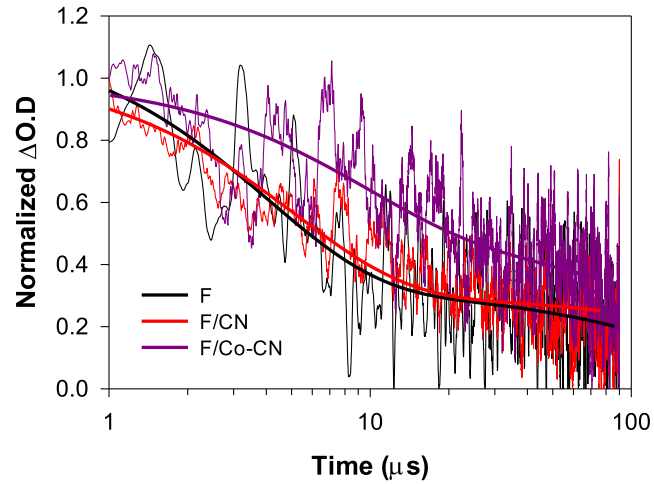

Fig. 6. Normalized transient absorption decays with F, F/CN, and F/Co-CN films at $\lambda = 600$ nm (excited at $\lambda = 355$ nm).

hematite, the Co-CN-deposited hematite films exhibited a prolonged decay curve of the trapped holes. CN exerted a similar yet less significant effect on the lifetime of the trapped holes. This indicates that the lifetime of the trapped holes increased in the presence of Co-CN.

Considering the one-electron oxidation potentials of the metal ions ($E^{\circ}(Ag^{2+/+}) = 1.98$ V; $E^{\circ}(Fe^{4+/3+}) = 2.2$ V; $E^{\circ}(Co^{3+/2+}) = 1.82$ V) [7,8,11], the photogenerated holes can be transferred from the valence band of hematite to the metal ions. Then, the hole-oxidized metal ions catalyze water oxidation and return to their original states. This mediated hole transfer occurs with the following J_{ph}: Co-CN > Fe-CN > Ag-CN > CN. For comparison, other seven metal ions were incorporated into CN and their effects on voltammograms were examined (Fig. S12). Among them, Ce(III) ($E^{\circ}(Ce^{4+/3+}) = 1.60$ V), Cu(II) ($E^{\circ}(Cu^{3+/2+}) = 2.41$ V), Ni(II) ($E^{\circ}(Ni^{3+/2+}) = 1.43$ V), and Mn(II) ($E^{\circ}(Mn^{3+/2+}) = 1.51$ V) enhanced PEC activity [63,64]. These metals have one-electron oxidation potentials similar to those of Ag(I), Fe(III), and Co(II). In contrast, Sn(IV), Zn(II), and Ru(III) with higher oxidation potentials than the hematite valence band did not show enhancement in PEC activity.

Finally, the hematite electrode with Co-CN overlayer was further loaded with FeNiOOH, one of the most representative oxygen evolution catalysts. Loading FeNiOOH to F/Co-CN not only enhanced J_{ph} from ~2.5–3.6 mA cm^{-1} at 1.23 V but also shifted E_{on} from 1.0 to 0.8 V (Fig. 7a). A similar effect was observed for other oxygen evolution catalysts such as CoOOH (Fig. S13) [5,9–11,13]. Both FeNiOOH and CoOOH catalysts significantly improved IPCE values up to ~18 % and 14 %, respectively, at $\lambda = 420$ nm (Fig. S14). A prolonged bulk photoelectrolysis with F/CN and F/Co-CN showed stable J_{ph} values of ~0.8 and 1.5 mA cm^{-2}, respectively, at 1.23 V over 24 h (Fig. 7a inset), while producing O_2 linearly with time (Fig. 7b). FEs for O_2 production were nearly constant over 24 h (Fig. 7c), indicating the durability of the photoanodes and stability in PEC water oxidation reaction. It is noteworthy that FEs with bare and CN-deposited hematite electrodes were similar at 25 %– 50 %, whereas F/Co-CN showed a significant high FE of ~75 %. These behaviors confirm again that the primary role of CN is enhancing charge separation via passivation of surface defects whereas the incorporated cobalt facilitates charge injection to interfacial water via mediating hole transfer. Loading FeNiOOH further facilitated O_2 production, with FE of > 95 % over 24 h.

4. Conclusions

This study demonstrated that deposition of metal-incorporated CN layers is effective in improving photoelectrochemical activity of hematite electrodes in alkaline solutions. The primary role of CN was found to

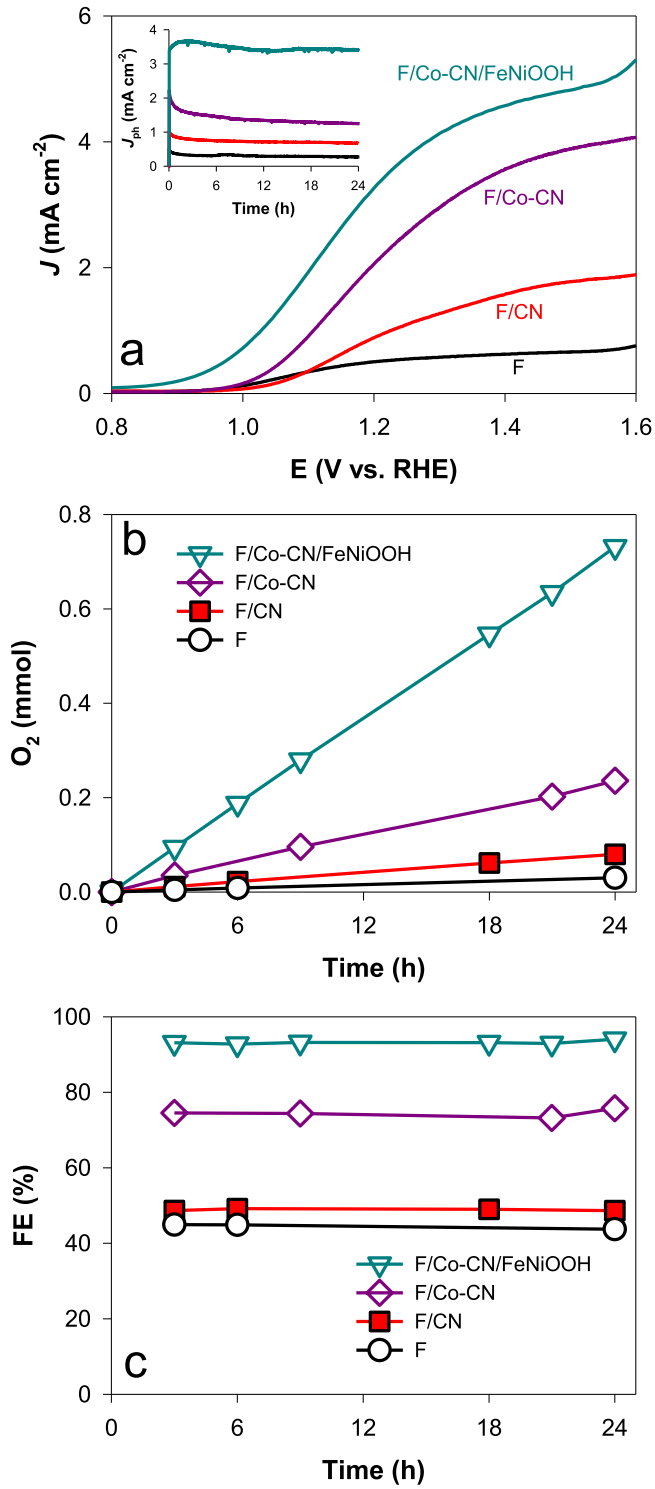

Fig. 7. Photoelectrochemical activities of bare and modified hematite electrodes in 1 M KOH solution under simulated sunlight. The electrolyte was purged with Ar gas over 30 min prior to irradiation. (a) Linear sweep voltammograms. Inset show the time-profiled J_{ph} values at 1.23 V. (b and c) O_2 evolution and Faradaic efficiencies with time at 1.23 V.

improve charge separation efficiency by passivating hematite surface and effectively blocking surface trap sites working as recombination centers. Meanwhile, the incorporated metal ions further contributed to reducing charge transfer resistance and mediating hole transfer to interfacial water. The redox potential of the incorporated metal was crucial in mediating hole transfer. These combined effects eventually led to enhancing the photoelectrochemical activity of hematite for oxygen evolution. The employed, one-step evaporation deposition method of ultra-thin M-CN film was facile and reliable, applicable to virtually all kinds of semiconductors, particularly suffering from many defects and poor stability.

CRediT authorship contribution statement

Tae Hwa Jeon: Methodology, Validation, Formal analysis, and Investigation. **Cheolwoo Park**: Validation, Formal analysis, Review & Editing. **Unseock Kang**: Validation, Formal analysis, Review & Editing. **Gun-hee Moon**: Validation, Formal analysis, Review & Editing. **Wooyul Kim**: Formal analysis, Review & Editing. **Hyunwoong Park**: Validation, Formal analysis, Resources, Writing –Original Draft, Writing – Review & Editing, Visualization, Supervision, Project administration, and Funding acquisition. **Wonyong Choi**: Validation, Formal analysis, Resources, Writing –Original Draft, Writing – Review & Editing, Visualization, Supervision, Project administration, and Funding acquisition.

Declaration of Competing Interest

The authors declare the following financial interests/personal relationships which may be considered as potential competing interests: Wonyong Choi and Hyunwoong Park reports financial support was provided by National Research Foundation of Korea.

Data availability

Data will be made available on request.

Acknowledgments

This research was financially supported by the Leading Researcher Program (NRF-2020R1A3B2079953), which was funded by the National Research Foundation of Korea (NRF). H.P. is grateful to the NRF (RS-2023–00254645).

Appendix A. Supporting information

Supplementary data associated with this article can be found in the online version at doi:10.1016/j.apcatb.2023.123167.

References

[1] C. Jiang, S.J. Moniz, A. Wang, T. Zhang, J. Tang, Photoelectrochemical devices for solar water splitting–materials and challenges, Chem. Soc. Rev. 46 (2017) 4645–4660.
[2] T.H. Jeon, M.S. Koo, H. Kim, W. Choi, Dual-functional photocatalytic and photoelectrocatalytic systems for energy-and resource-recovering water treatment, ACS Catal. 8 (2018) 11542–11563.
[3] M. Faraji, M. Yousefi, S. Yousefzadeh, M. Zirak, N. Naseri, T.H. Jeon, W. Choi, A. Z. Moshfegh, Two-dimensional materials in semiconductor photoelectrocatalytic systems for water splitting, Energy Environ. Sci. 12 (2019) 59–95.
[4] C. Ding, J. Shi, Z. Wang, C. Li, Photoelectrocatalytic water splitting: significance of cocatalysts, electrolyte, and interfaces, ACS Catal. 7 (2016) 675–688.
[5] H.W. Jeong, W.-S. Chae, B. Song, C.-H. Cho, S.-H. Baek, Y. Park, H. Park, Optical resonance and charge transfer behavior on patterned WO_3 microdisc arrays, Energy Environ. Sci. 9 (2016) 3143–3150.
[6] N.C. Deb Nath, S.Y. Choi, H.W. Jeong, J.-J. Lee, H. Park, Stand-alone photoconversion of carbon dioxide on copper oxide wire arrays powered by tungsten trioxide/dye-sensitized solar cell dual absorbers, Nano Energy 25 (2016) 51–59.
[7] T.H. Jeon, S. Han, B. Kim, C. Park, W. Kim, H. Park, W. Choi, High-valent iron redox-mediated photoelectrochemical water oxidation, ACS Energy Lett. 7 (2022) 59–66.
[8] T.H. Jeon, D. Monllor-Satoca, G.-H. Moon, W. Kim, H.-I. Kim, D.W. Bahnemann, H. Park, W. Choi, Ag(I) ions working as a hole-transfer mediator in photoelectrocatalytic water oxidation on WO_3 film, Nat. Commun. 11 (2020) 967.
[9] H.W. Jeong, T.H. Jeon, J.S. Jang, W. Choi, H. Park, Strategic modification of $BiVO_4$ for improving photoelectrochemical water oxidation performance, J. Phys. Chem. C 117 (2013) 9104–9112.

[10] S.K. Choi, W. Choi, H. Park, Solar water oxidation using nickel-borate coupled $BiVO_4$ photoelectrodes, Phys. Chem. Chem. Phys. 15 (2013) 6499–6507.
[11] T.H. Jeon, W. Choi, H. Park, Cobalt-phosphate complexes catalyze the photoelectrochemical water oxidation of $BiVO_4$ electrodes, Phys. Chem. Chem. Phys. 13 (2011) 21392–21401.
[12] T.H. Jeon, W. Choi, H. Park, Photoelectrochemical and photocatalytic behaviors of hematite-decorated titania nanotube arrays: energy level mismatch versus surface specific reactivity, J. Phys. Chem. C 115 (2011) 7134–7142.
[13] T.H. Jeon, G.-H. Moon, H. Park, W. Choi, Ultra-efficient and durable photoelectrochemical water oxidation using elaborately designed hematite nanorod arrays, Nano Energy 39 (2017) 211–218.
[14] A. Annamalai, A. Subramanian, U. Kang, H. Park, S.H. Choi, J.S. Jang, Activation of hematite photoanodes for solar water splitting: Effect of FTO deformation, J. Phys. Chem. C 119 (2015) 3810–3817.
[15] A. Bak, W. Choi, H. Park, Enhancing the photoelectrochemical performance of hematite (α-Fe_2O_3) electrodes by cadmium incorporation, Appl. Catal. B-Environ. 110 (2011) 207–215.
[16] J.H. Kennedy, K.W. Frese, Photooxidation of water at α-Fe_2O_3 electrodes, J. Electrochem. Soc. 125 (1978) 709–714.
[17] S. Piccinin, The band structure and optical absorption of hematite (α-Fe_2O_3): a first-principles GW-BSE study, Phys. Chem. Chem. Phys. 21 (2019) 2957–2967.
[18] K. Sivula, F. Le Formal, M. Grätzel, Solar water splitting: progress using hematite (α-Fe_2O_3) photoelectrodes, ChemSusChem 4 (2011) 432–449.
[19] S.R. Pendlebury, X. Wang, F. Le Formal, M. Cornuz, A. Kafizas, S.D. Tilley, M. Grätzel, J.R. Durrant, Ultrafast charge carrier recombination and trapping in hematite photoanodes under applied bias, J. Am. Chem. Soc. 136 (2014) 9854–9857.
[20] N.J. Cherepy, D.B. Liston, J.A. Lovejoy, H. Deng, J.Z. Zhang, Ultrafast studies of photoexcited electron dynamics in γ-and α-Fe_2O_3 semiconductor nanoparticles, J. Phys. Chem. B 102 (1998) 770–776.
[21] F. Morin, Electrical properties of α-Fe_2O_3 and α-Fe_2O_3 containing titanium, Phys. Rev. 83 (1951) 1005.
[22] M.P. Dare-Edwards, J.B. Goodenough, A. Hamnett, P.R. Trevellick, Electrochemistry and photoelectrochemistry of iron (III) oxide, J. Chem. Soc. Faraday Trans. 1 Phys. Chem. Condens. Phases 79 (1983) 2027–2041.
[23] T. Lindgren, H. Wang, N. Beermann, L. Vayssieres, A. Hagfeldt, S.-E. Lindquist, Aqueous photoelectrochemistry of hematite nanorod array, Sol. Energy Mater. Sol. Cells 71 (2002) 231–243.
[24] T.H. Jeon, A.D. Bokare, D.S. Han, A. Abdel-Wahab, H. Park, W. Choi, Dual modification of hematite photoanode by Sn-doping and Nb_2O_5 layer for water oxidation, Appl. Catal. B 201 (2017) 591–599.
[25] J. Xiao, C. Li, X. Jia, B. Du, R. Li, B. Wang, Enabling high low-bias performance of Fe_2O_3 photoanode for photoelectrochemical water splitting, J. Colloid Interface Sci. 633 (2023) 555–565.
[26] J.H. Kim, J.-W. Jang, Y.H. Jo, F.F. Abdi, Y.H. Lee, R. Van De Krol, J.S. Lee, Hetero-type dual photoanodes for unbiased solar water splitting with extended light harvesting, Nat. Commun. 7 (2016) 13380.
[27] D.K. Zhong, M. Cornuz, K. Sivula, M. Grätzel, D.R. Gamelin, Photo-assisted electrodeposition of cobalt–phosphate (Co–Pi) catalyst on hematite photoanodes for solar water oxidation, Energy Environ. Sci. 4 (2011) 1759–1764.
[28] Z. Luo, T. Wang, J. Zhang, C. Li, H. Li, J. Gong, Dendritic hematite nanoarray photoanode modified with a conformal titanium dioxide interlayer for effective charge collection, Angew. Chem. Int. Ed. 56 (2017) 12878–12882.
[29] H. Chai, L. Gao, J. Jin, Revealing the essential role of iron phosphide and its surface-evolved species in the photoelectrochemical water oxidation by Gd-doped hematite photoanode, ChemSusChem 15 (2022), e202201030.
[30] H. Shuwanto, H. Abdullah, D.-H. Kuo, Nanostructuring Bi-Doped alpha-Fe_2O_3 thin-layer photoanode to advance the water oxidation performance, ACS Appl. Mater. Interfaces 5 (2022) 9902–9913.
[31] F. Le Formal, N. Tetreault, M. Cornuz, T. Moehl, M. Grätzel, K. Sivula, Passivating surface states on water splitting hematite photoanodes with alumina overlayers, Chem. Sci. 2 (2011) 737–743.
[32] X. Yang, R. Liu, C. Du, P. Dai, Z. Zheng, D. Wang, Improving hematite-based photoelectrochemical water splitting with ultrathin TiO_2 by atomic layer deposition, ACS Appl. Mater. Interfaces 6 (2014) 12005–12011.
[33] R. Liu, Z. Zheng, J. Spurgeon, X. Yang, Enhanced photoelectrochemical water-splitting performance of semiconductors by surface passivation layers, Energy Environ. Sci. 7 (2014) 2504–2517.
[34] L.K. Dhandole, H.H. Lee, W.-S. Chae, J.S. Jang, J.S. Lee, Self-motivated, thermally oxidized hematite nanoflake photoanodes: effects of pre-polishing and ZrO_2 passivation layer, J. Energy Chem. 65 (2022) 415–423.
[35] W. Kim, T. Tachikawa, D. Monllor-Satoca, H.-I. Kim, T. Majima, W. Choi, Promoting water photooxidation on transparent WO_3 thin films using an alumina overlayer, Energy Environ. Sci. 6 (2013) 3732–3739.
[36] F. Li, J. Jian, S. Wang, Z. Zhang, L. Jia, X. Guan, Y. Xu, H. Wang, TiO_2 passivation layers with laser derived p-n heterojunctions enable boosted photoelectrochemical performance of α-Fe_2O_3 photoanodes, Chem. Eng. J. 461 (2023), 141872.
[37] A. Naseri, M. Samadi, A. Pourjavadi, A.Z. Moshfegh, S. Ramakrishna, Graphitic carbon nitride (gC_3N_4)-based photocatalysts for solar hydrogen generation: recent advances and future development directions, J. Mater. Chem. A 5 (2017) 23406–23433.
[38] G.-H. Moon, M. Fujitsuka, S. Kim, T. Majima, X. Wang, W. Choi, Eco-friendly photochemical production of H_2O_2 through O_2 reduction over carbon nitride frameworks incorporated with multiple heteroelements, ACS Catal. 7 (2017) 2886–2895.
[39] C.H. Choi, L. Lin, S. Gim, S. Lee, H. Kim, X. Wang, W. Choi, Polymeric carbon nitride with localized aluminum coordination sites as a durable and efficient photocatalyst for visible light utilization, ACS Catal. 8 (2018) 4241–4256.
[40] W.-J. Ong, L.-L. Tan, Y.H. Ng, S.-T. Yong, S.-P. Chai, Graphitic carbon nitride (g-C_3N_4)-based photocatalysts for artificial photosynthesis and environmental remediation: are we a step closer to achieving sustainability? Chem. Rev. 116 (2016) 7159–7329.
[41] Y. Li, R. Wang, H. Li, X. Wei, J. Feng, K. Liu, Y. Dang, A. Zhou, Efficient and stable photoelectrochemical seawater splitting with TiO_2@g-C_3N_4 nanorod arrays decorated by Co-Pi, J. Phys. Chem. C 119 (2015) 20283–20292.
[42] S.-S. Yi, J.-M. Yan, Q. Jiang, Carbon quantum dot sensitized integrated Fe_2O_3@g-C_3N_4 core–shell nanoarray photoanode towards highly efficient water oxidation, J. Mater. Chem. A 6 (2018) 9839–9845.
[43] H. Li, F. Zhao, J. Zhang, L. Luo, X. Xiao, Y. Huang, H. Ji, Y. Tong, A gC_3N_4/WO_3 photoanode with exceptional ability for photoelectrochemical water splitting, Mater. Chem. Front. 1 (2017) 338–342.
[44] S. Kim, G.-H. Moon, H. Kim, Y. Mun, P. Zhang, J. Lee, W. Choi, Selective charge transfer to dioxygen on KPF_6-modified carbon nitride for photocatalytic synthesis of H_2O_2 under visible light, J. Catal. 357 (2018) 51–58.
[45] P. Zhang, D. Sun, A. Cho, S. Weon, S. Lee, J. Lee, J.W. Han, D.-P. Kim, W. Choi, Modified carbon nitride nanozyme as bifunctional glucose oxidase-peroxidase for metal-free bioinspired cascade photocatalysis, Nat. Commun. 10 (2019) 940.
[46] H.L. Peng, F.F. Liu, X.J. Liu, S.J. Liao, C.H. You, X.L. Tian, H.X. Nan, F. Luo, H. Y. Song, Z.Y. Fu, P.Y. Huang, Effect of transition metals on the structure and performance of the doped carbon catalysts derived from polyaniline and melamine for ORR application, ACS Catal. 4 (2014) 3797–3805.
[47] X. Wang, S. Blechert, M. Antonietti, Polymeric graphitic carbon nitride for heterogeneous photocatalysis, ACS Catal. 2 (2012) 1596–1606.
[48] Q. Ruan, W. Luo, J. Xie, Y. Wang, X. Liu, Z. Bai, C.J. Carmalt, J. Tang, A nanojunction polymer photoelectrode for efficient charge transport and separation, Angew. Chem. Int. Ed. 56 (2017) 8221–8225.
[49] D.A. Salvatore, K.E. Dettelbach, J.R. Hudkins, C.P. Berlinguette, Near-infrared–driven decomposition of metal precursors yields amorphous electrocatalytic films, Sci. Adv. 1 (2015), e1400215.
[50] P. Sun, X. He, W. Wang, J. Ma, Y. Sun, G. Lu, Template-free synthesis of monodisperse α-Fe_2O_3 porous ellipsoids and their application to gas sensors, CrystEngComm 14 (2012) 2229–2234.
[51] S.K. Choi, W.-S. Chae, B. Song, C.-H. Choi, J. Choi, D.S. Han, W. Choi, H. Park, Photoelectrochemical hydrogen production on silicon microwire arrays overlaid with ultrathin titanium nitride, J. Mater. Chem. A 4 (2016) 14008–14016.
[52] S.K. Choi, U. Kang, S. Lee, D.J. Ham, S.M. Ji, H. Park, Sn-coupled p-Si nanowire arrays for solar formate production from CO_2, Adv. Energy Mater. 4 (2014), 1301614.
[53] S.K. Choi, G. Piao, W. Choi, H. Park, Highly efficient hydrogen production using p-Si wire arrays and NiMoZn heterojunction photocathodes, Appl. Catal., B 217 (2017) 615–621.
[54] T.H. Jeon, H.I. Choi, H. Park, H.I. Kim, W. Choi, Synergistic effect of Sn doping and hydrogenation on hematite electrodes for photoelectrochemical water oxidation, Mater. Chem. Front. 5 (2021) 6592–6602.
[55] S. Kim, D.S. Han, H. Park, Reduced titania nanorods and Ni-Mo-S catalysts for photoelectrocatalytic water treatment and hydrogen production coupled with desalination, Appl. Catal. B 284 (2021), 119745.
[56] S.Y. Choi, S. Kim, K.J. Lee, J.Y. Kim, D.S. Han, H. Park, Solar hydrogen peroxide production on carbon nanotubes wired to titania nanorod arrays catalyzing As(III) oxidation, Appl. Catal. B 952 (2019) 55–61.
[57] U. Kang, H. Park, Lithium ion-inserted TiO_2 nanotube array photoelectrocatalysts, Appl. Catal. B 140 (2013) 233–240.
[58] H.W. Jeong, K.J. Park, D.S. Han, H. Park, High efficiency solar chemical conversion using electrochemically disordered titania nanotube arrays transplanted onto transparent conductive oxide electrodes, Appl. Catal. B 307 (2018) 131–139.
[59] G.W. An, L.K. Dhandole, H. Park, M.A. Mahadik, J.S. Jang, Enhanced charge transfer process in morphology restructured TiO_2 nanotubes via hydrochloric acid assisted one step in-situ hydrothermal approach, ChemCatChem 11 (2019) 5605–5614.
[60] S. Shen, S.A. Lindley, X. Chen, J.Z. Zhang, Hematite heterostructures for photoelectrochemical water splitting: rational materials design and charge carrier dynamics, Energy Environ. Sci. 9 (2016) 2744–2775.
[61] G.X. Pei, H.J. Wijten, B.M. Weckhuysen, Probing the dynamics of photogenerated holes in doped hematite photoanodes for solar water splitting using transient absorption spectroscopy, Phys. Chem. Chem. Phys. 20 (2018) 9806–9811.
[62] M. Barroso, C.A. Mesa, S.R. Pendlebury, A.J. Cowan, T. Hisatomi, K. Sivula, M. Grätzel, D.R. Klug, J.R. Durrant, Dynamics of photogenerated holes in surface modified α-Fe_2O_3 photoanodes for solar water splitting, Proc. Natl. Acad. Sci. USA 109 (2012) 15640–15645.
[63] A.J. Bard, Standard Potentials in Aqueous Solution, Routledge, 2017.
[64] D. González-Flores, K. Klingan, P. Chernev, S. Loos, M.R. Mohammadi, C. Pasquini, P. Kubella, I. Zaharieva, R.D. Smith, H. Dau, Nickel-iron catalysts for electrochemical water oxidation–redox synergism investigated by in situ X-ray spectroscopy with millisecond time resolution, Sustain. Energy Fuels 2 (2018) 1986–1994.